

An analytical analysis of the pullout behaviour of reinforcements of MSE structures

Feifan Ren^{*1,2}, Guan Wang^{3a} and Bin Ye^{1,2b}

¹Key Laboratory of Geotechnical and Underground Engineering of the Ministry of Education, Tongji University, Shanghai 200092, China .

²Department of Geotechnical Engineering, College of Civil Engineering, Tongji University, Shanghai 200092, China

³School of Environment and Architecture, University of Shanghai for Science and Technology, Shanghai 200093, China

(Received June 20, 2016, Revised June 28, 2017, Accepted July 21, 2017)

Abstract. Pullout tests are usually employed to determine the ultimate bearing capacity of reinforced soil, and the load-displacement curve can be obtained easily. This paper presents an analytical solution for predicting the full-range mechanical behavior of a buried planar reinforcement subjected to pullout based on a bi-linear bond-slip model. The full-range behavior consists of three consecutive stages: elastic stage, elastic-plastic stage and debonding stage. For each stage, closed-form solutions for the load-displacement relationship, the interfacial slip distribution, the interfacial shear stress distribution and the axial stress distribution along the planar reinforcement were derived. The ultimate load and the effective bond length were also obtained. Then the analytical model was calibrated and validated against three pullout experimental tests. The predicted load-displacement curves as well as the internal displacement distribution are in closed agreement with test results. Moreover, a parametric study on the effect of anchorage length, reinforcement axial stiffness, interfacial shear stiffness and interfacial shear strength is also presented, providing insights into the pullout behaviour of planar reinforcements of MSE structures.

Keywords: planar reinforcements; analytical solution; pullout behavior; bond-slip model; parametric study

1. Introduction

Mechanically stabilized earth (MSE) structures have gained wide acceptance as means of improving the stability of slopes, retaining walls and embankments (Wilson-Fahmy and Koerner 1993, Karpurapu and Bathurst 1995, Yang *et al.* 2010). A MSE structure is typically composed of soil, reinforcements (geogrid, geotextile, and metal strip etc.) and facing pannels, and reinforcements are usually under tension. When a MSE structure is designed, the values of soil-reinforcement interface shear strength parameters are usually to be required. Conventional design uses limit equilibrium methods which assume that all of the points along the reinforcements reach the limit state simultaneously, and the interface direct shear test is usually adopted to determine these strength parameters. However, it has been proved that the shear stresses developed along reinforcements of MSE structures are not uniform by many researchers, and the friction along reinforcements will develop progressively, with the front end of the reinforcement reaching very large displacement while the rear end may not even feel the presence of the pullout effect (Alobaidi *et al.* 1997, Sieira *et al.* 2009).

Pullout tests, which are acknowledged to more closely simulate in-situ condition, are usually employed to determine the ultimate pullout capacity of reinforced soil, and the load-displacement curve can be obtained easily. Meanwhile, the strain distribution can also be acquired by using strain gauges mounted on the surface of reinforcement. Since the application of MSE structures started, a large number of laboratory experiments have been carried out to investigate the mechanical behavior of reinforcements under tension (Palmeira 2009, Sieira *et al.* 2009, Abdi and Zandieh 2014, Bathurst and Ezzein 2015, Ferreira and Zornberg 2015, Wang *et al.* 2016). It has been found that reinforcements often fail by debonding at the reinforcement-soil interface, although rupture of reinforcements has also been reported in a few cases. For the debonding failure, the determination of the accurate distribution of the interface shear stress along the bonded length is crucial for predicting the ultimate bearing capacity and for making an optimal design. In spite of this understanding, a limited number of analytical studies have been reported in literature. For instance, Abramento and Whittle (1995) described an analysis for predicting the tensile stress distribution and load-elongation response in pullout tests performed on thin, extensible, planar soil reinforcements, however, it was simply assumed in the proposed analysis that the axial stresses in the soil and in the inclusion are functions of x (horizontal position) only. Bergado *et al.* (2001) and Teerawattanasuk *et al.* (2003) developed an analytical model to predict the in-soil pullout resistance from the deformation of the hexagonal wire mesh in both pullout and lateral directions. Weerasekara and Wijewickreme (2010) proposed an analytical model

*Corresponding author, Assistant Professor

E-mail: feifan_ren@tongji.edu.cn

^aAssociate Professor

E-mail: wangguan@usst.edu.cn

^bAssociate Professor

E-mail: yebin@tongji.edu.cn

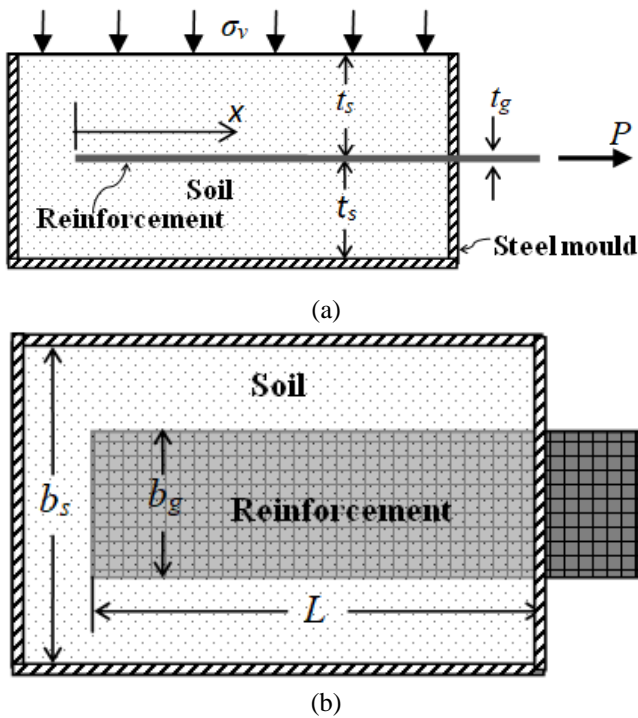


Fig. 1 Pullout test, (a) Elevation and (b) Plan

combining the nonlinear responses of the geotextile and soil-geotextile interface characteristics. However, the distinct closed-form solutions for the interfacial slip, the interfacial shear stress and the axial stress in the geogrid were not obtained, and iterative computation need to be used to solve the interaction problem.

In this paper, based on a bi-linear bond-slip model, a closed-form analytical solution is developed first to present the response of a buried planar reinforcement subjected to pullout, and then using the analytical solution, a method is proposed to determine the interface friction parameters by the load-displacement curve. On these bases, a comparison is made between predicted and measured pullout force-displacement relationship and internal displacement distribution along the reinforcement. Finally, a parametric study is carried out to evaluate the influence of stiffness and length of the reinforcement on the pullout behavior of the MSE structure. The main advantage of the proposed analytical method is its simplicity, which enables clear physical interpretation of the effects of individual parameters and avoids the complexities associated with nonlinear numerical analyses using interfacial elements.

2. The pullout tests and an idealized model

Laboratory tests have been conducted to evaluate the load-carrying capacity and related mechanical parameters of reinforcements in MSE structures. Fig. 1 illustrates a pullout test of the planar reinforcement which is capable of accurately evaluating load-carrying capacity of the tested reinforcement. It is known that the ultimate failure may occur: (a) in the reinforcement, (b) at the reinforcement-soil interface. This paper is concerned with the very common debonding failure at the reinforcement-soil interface. Under

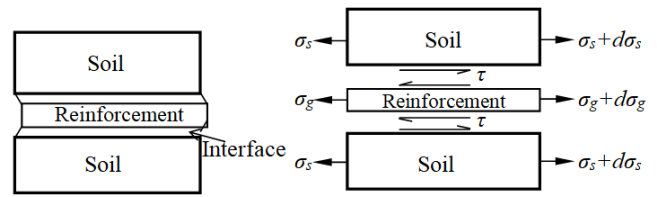


Fig. 2 Idealised model: deformation and stresses

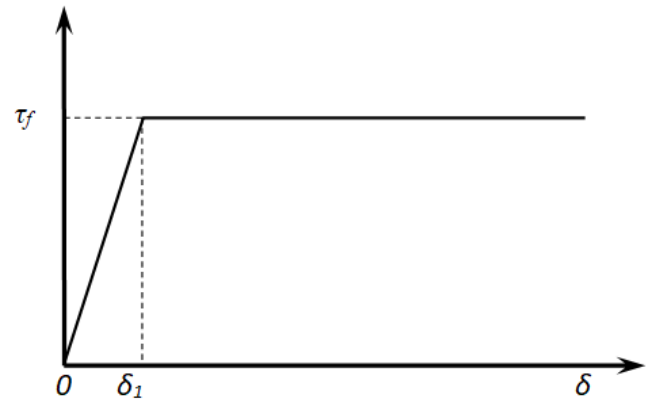


Fig. 3 Bi-linear bond-slip model

the debonding failures, the deformation of the surrounding soil is often negligible due to boundary conditions, which is constrained by a steel mould (Fig. 1). As a result, the reinforcement can be assumed to be under unidirectional tension and the reinforcement-soil interface under interfacial shear deformation only, leading to an idealized model as in Fig. 2 when the failure occurs due to debonding at the reinforcement-soil interface. It should be noted that the zero thickness interface represents the materials adjacent to the critical interface where debonding failure occurs. All deformations in the surrounding soil are lumped in the interface in this idealized model. It is also assumed that the pullout force P is horizontal so that the stress in the protruding length of the reinforcement is uniform.

3. Bi-linear bond-slip model

There are several types of reinforcements usually used in MSE structures, such as metallic strips, geotextiles and geogrids etc. Among them, only geotextiles are rigorously sheet-like reinforcements, metallic strips can be treated as sheet-like reinforcements with a certain width, and their bearing capacity under pullout conditions is mainly provided by the interfacial frictional force between the reinforcement and the soil. However, geogrids, with open aperture, derive their anchorage capacity through both friction and bearing resistances (Wilson-Fahmy *et al.* 1994). For simplicity, the geogrid can be treated as a sheet-like reinforcement without apertures, and geogrid thickness t_g is obtained by the equivalent stiffness method which is usually used in pile foundation analysis.

It has been found in many experimental studies that the relationship between shear stress and shear slip follows the theory of perfect-plasticity (Alobaidi *et al.* 1997, Sieira *et al.* 2009, Xu *et al.* 2013). Therefore, a simple bi-linear bond-slip model is adopted in this paper as shown in Fig. 3. It has an ascending part up to the peak stress at (τ_f, δ_1)

followed by a horizontal part representing that the shear stress will maintain the peak stress after complete debonding. The bi-linear bond-slip model is assumed as a material property and all the parameters can be calibrated from pullout tests, as discussed later in this paper.

The bi-linear bond-slip model as shown in Fig. 3 can be mathematically expressed as

$$\tau(\delta) = \begin{cases} \frac{\tau_f}{\delta_1} \delta & \text{for } 0 \leq \delta \leq \delta_1 \text{ (a)} \\ \tau_f & \text{for } \delta \geq \delta_1 \text{ (b)} \end{cases} \quad (1)$$

It should be noted that τ_f is generally constant for a given burial depth in the pullout test, and it can be expressed as

$$\tau_f = N \operatorname{tg} \theta \quad (2)$$

where N is the vertical earth pressure, $\operatorname{tg} \theta$ is the interface friction coefficient between soil and reinforcement, and the value of θ is a function of the confining effective stress and density of the soil.

However, there is an evidence from pullout tests performed on MSE that the frictional resistance at buried interfaces may often be several magnitudes greater than τ_f derived from Eq. (2) (i.e., shear dilation) (Schlosser and Elias 1978, Ingold 1982). This phenomenon can be explained such that the normal stress N is usually increased during pullout tests due to shear-induced volumetric expansion of soil particles, especially for compacted soil. Therefore, it is very difficult to accurately assess the value of τ_f using Eq. (2).

4. Governing equations

Based on the assumptions stated in Section 2, the following fundamental equations can be established based on force equilibrium considerations in Fig. 2

$$\frac{d\sigma_g}{dx} - \frac{2\tau}{t_g} = 0 \quad (3)$$

where τ is the shear stress at the interface, σ_g is the axial stress in the planar reinforcement.

The constitutive equations for the interface and the reinforcement are

$$\tau = \tau(\delta) \quad (4)$$

$$\sigma_g = E_g \frac{du_g}{dx} \quad (5)$$

where E_g is the Young's modulus of the reinforcement, and the function $\tau(\delta)$ relates the local interfacial shear stress τ to the local shear slip δ as in Eq. (1). The shear slip δ is defined as the relative displacement between the reinforcement and its surrounding soil. Based on the assumption that all deformation in the surrounding soil is lumped onto the interface, the shear slip δ equals the axial displacement of the reinforcement u_g

$$\delta = u_g \quad (6)$$

Substituting Eqs. (4)-(6) into Eq. (3), the governing equation of the reinforced soil and the axial stress in the reinforcement can be expressed as

$$\frac{d^2 \delta}{dx^2} - \frac{\delta_1}{\tau_f} \lambda^2 \tau(\delta) = 0 \quad (7)$$

$$\sigma_g = \frac{2\tau_f}{\delta_1 t_g \lambda^2} \frac{d\delta}{dx} \quad (8)$$

where

$$\lambda^2 = \frac{2\tau_f}{\delta_1 E_g t_g} \quad (9)$$

The governing differential Eq. (7) can be solved once the bond-slip model represented by $\tau(\delta)$ in Eq. (1) is defined.

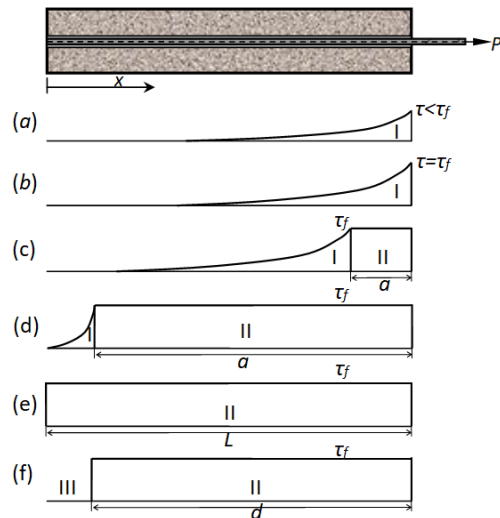


Fig. 4 Evolution of interfacial shear stress distribution and propagation of debonding. (a)-(b), elastic stage, (c)-(d): elastic-plastic stage and (e)-(f) debonding stage, I, II, III represent elastic, plastic and debonding stress state respectively

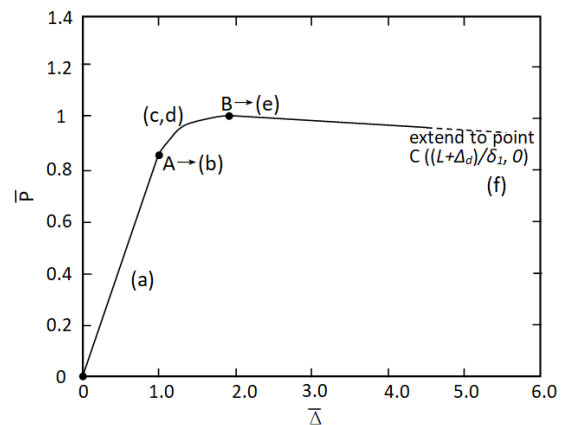


Fig. 5 Typical full-range theoretical non-dimensional load-displacement curve

5. Analysis of the full-range behavior and derivation of analytical solutions

Using the bi-linear bond-slip model defined above, the shear slip and shear stress distributions along the interface, the axial stress in the reinforcement, and the load-displacement relation can be obtained by solving the governing Eq. (7) for every loading stage. Fig. 4 illustrates the evolution of interfacial shear stress distribution when the bond length is significantly longer than the effective bond length to allow for transfer of the ultimate load (the peak value of pullout load). Fig. 5 shows the load-displacement curve corresponding to Fig. 4.

5.1 Elastic stage

Under a small pullout force, there is no plastic deformation along the reinforcement-soil interface, so the entire length of the interface remains elastic (Fig. 4(a) and segment OA in Fig. 5). This is true until the interfacial shear stress reaches τ_f at $x=L$. Substituting Eq. (1a) for the case of $0 \leq \delta \leq \delta_1$ into Eq. (7), the differential equation for the elastic stage can be obtained

$$\frac{d^2 \delta}{dx^2} - \lambda^2 \delta = 0 \quad (10)$$

Considering the following boundary conditions

$$\sigma_g = 0 \quad \text{at } x = 0 \quad (11)$$

$$\sigma_g = \frac{P}{b_g t_g} \quad \text{at } x = L \quad (12)$$

The interfacial slip, the interfacial shear stress and the axial stress in the reinforcement can be obtained by solving Eq. (10)

$$\delta = \frac{P \delta_1 \lambda \cosh(\lambda x)}{2 \tau_f b_g \sinh(\lambda L)} \quad (13)$$

$$\tau = \frac{P \lambda \cosh(\lambda x)}{2 b_g \sinh(\lambda L)} \quad (14)$$

$$\sigma_g = \frac{P \sinh(\lambda x)}{t_g b_g \sinh(\lambda L)} \quad (15)$$

The slip at the loaded end with $x=L$ is defined as the displacement of the reinforcement joint and is denoted as Δ . The following load-displacement expression can then be obtained from Eq. (13)

$$P = \frac{2 \tau_f b_g \tanh(\lambda L)}{\lambda \delta_1} \Delta \quad (16)$$

Introducing the normalised load and displacement

$$\bar{P} = \frac{P}{2 \tau_f b_g L} \quad (17)$$

$$\bar{\Delta} = \frac{\Delta}{\delta_1} \quad (18)$$

Eq. (16) is simplified as

$$\bar{P} = \frac{\tanh(\lambda L)}{\lambda L} \bar{\Delta} \quad \text{for } 0 \leq \bar{\Delta} \leq 1 \quad (19)$$

It may be noted that in the elastic stage, only part of the interface is significantly loaded with the stresses elsewhere being very small (Figs. 4(a)-(b)). As in the study of Ren *et al.* (2010), the effective bond length is defined as the bond length over which the interfacial shear stresses offer a total resistance of at least 97% of the applied load for a joint with an infinite bond length. Based on this definition and considering that $\tanh(2)$ is about 0.97, the effective bond length in the elastic stage becomes independent of the load level and is given by

$$l_{e,e} = 2 / \lambda \quad (20)$$

The elastic stage ends when the shear stress reaches the bond shear strength τ_f at a displacement of δ_1 at $x=L$ (Fig. 4(b)). Equating Δ to δ_1 in Eq. (16), the load at the initiation of the elastic-plastic stage is found to be

$$P_{ela-pla} = \frac{2 \tau_f b_g \tanh(\lambda L)}{\lambda} \quad (21)$$

or an infinite bond length, because $\lim_{L \rightarrow \infty} \tanh(\lambda L) = 1$, Eq. (21) reduces to

$$P_{ela-pla} = \frac{2 \tau_f b_g}{\lambda} \quad (22)$$

5.2 Elastic-plastic stage

As the pullout force increases, plastic deformation commences at the loaded end ($x=L$) and the shear stress reaches its peak value and then remains constant. The peak shear stress τ_f is transferred towards the embedded end, and part of the interface near the loaded end enters the plastic state (state II) as shown in Fig. 4(c). With the development of the plastic length a , the load P continues to increase because greater interface is mobilized to resist the pullout force. At the end of this stage (Fig. 4(d) and Point 'B' in Fig. 5), P reaches the debonding load P_{deb} . The load-displacement curve in this stage is represented by segment AB in Fig. 5.

Substituting Eqs. (1(a) and 1(b)) into Eq. (7), the following differential equations for the elastic-plastic stage can be obtained

$$\frac{d^2 \delta}{dx^2} - \lambda^2 \delta = 0 \quad \text{when } 0 \leq \delta \leq \delta_1 \quad (23)$$

$$\frac{d^2 \delta}{dx^2} - \lambda^2 \delta_1 = 0 \quad \text{when } \delta \geq \delta_1 \quad (24)$$

The boundary conditions are

$$\sigma_g = 0 \quad \text{at } x = 0 \quad (25)$$

$$\sigma_g \text{ is continuous} \quad \text{at } x = L - a \quad (26)$$

$$\delta = \delta_1 \quad \text{or } \tau = \tau_f \quad \text{at } x = L - a \quad (27)$$

$$\sigma_g = \frac{P}{t_g b_g} \quad \text{at } x = L \quad (28)$$

The solution for the elastic region of the interface with $0 \leq \delta \leq \delta_1$ (or $0 \leq x \leq L - a$) is

$$\delta = \frac{\delta_1 \cosh(\lambda x)}{\cosh[\lambda(L - a)]} \quad (29)$$

$$\tau = \frac{\tau_f \cosh(\lambda x)}{\cosh[\lambda(L - a)]} \quad (30)$$

$$\sigma_g = \frac{2\tau_f \sinh(\lambda x)}{\lambda t_g \cosh[\lambda(L - a)]} \quad (31)$$

The solution for the plastic region with $\delta \geq \delta_1$ (or $L - a \leq x \leq L$) is

$$\delta = \frac{1}{2} \lambda^2 \delta_1 x^2 + \lambda \delta_1 \{ \tanh[\lambda(L - a)] - \lambda(L - a) \} x + \delta_1 + \frac{1}{2} \lambda^2 \delta_1 (L - a)^2 - \lambda \delta_1 (L - a) \tanh[\lambda(L - a)] \quad (32)$$

$$\tau = \tau_f \quad (33)$$

$$\sigma_g = \frac{2\tau_f}{\lambda t_g} \{ \lambda x + \tanh[\lambda(L - a)] - \lambda(L - a) \} \quad (34)$$

Substituting Eq. (28) into Eq. (34) gives

$$P = \frac{2\tau_f b_g}{\lambda} \{ \tanh[\lambda(L - a)] + \lambda a \} \quad (35)$$

The displacement at $x=L$ can be obtained from Eq. (32) as

$$\Delta = \delta_1 + \frac{1}{2} \lambda^2 \delta_1 a^2 + \lambda \delta_1 a \tanh[\lambda(L - a)] \quad (36)$$

Substituting Eq. (35) and Eq. (36) into Eq. (17) and Eq. (18) respectively, and the normalized load and displacement can be expressed as

$$\bar{P} = \frac{\tanh[\lambda(L - a)] + \lambda a}{\lambda L} \quad (37)$$

$$\bar{\Delta} = 1 + \frac{1}{2} \lambda^2 a^2 + \lambda a \tanh[\lambda(L - a)] \quad (38)$$

The distribution of the interfacial shear stress during the elastic-plastic stage is illustrated in Figs. 4(c) and 4(d). During this stage, the load-displacement curve plotted from Eqs. (37) and (38) is shown as segment AB in Fig. (5). Obviously, the joint reaches its ultimate load at the end of this stage. P reaches its maximum when the derivative of Eq. (35) with respect to a equals zero. Therefore, a at the ultimate load can be found to be L .

Substituting the equation $a=L$ into Eq. (35) yields Eq. (36), which is very familiar.

$$P_u = 2\tau_f b_g L \quad (39)$$

5.3 Debonding stage

This stage starts when the elastic zone disappears (Point 'B' in Fig. 5). In this stage, the load-carrying capacity is solely provide by the maximum friction (Fig. 4(e) and 4(f)). The displacement at the end of the elastic-plastic stage, denoted by Δ_d , can be obtained from Eq. (36) by setting $a=L$

$$\Delta_d = \delta_1 + \frac{1}{2} \lambda^2 \delta_1 L^2 \quad (40)$$

The pull-out displacement Δ after this varies from Δ_d at the beginning of this stage to $L + \Delta_d$ when the reinforcement is completely pulled out. Neglecting the effect of the reinforcement elongation which is very small compared with Δ at this stage, the load-displacement relationship at debonding stage can be expressed as

$$P = 2b_g \tau_f (L + \Delta_d - \Delta) \quad (41)$$

5.4 Characteristic points on the load-displacement curve

The above analysis shows that the full-range mechanical behaviour of reinforcements under tension consists of three distinct stages as depicted in Fig. 5. The important points are Point 'A' corresponding to the initiation of the interface plastic deformation, Point 'B' corresponding to the initiation of debonding and the ultimate load. These two points may be identified from an experimental load-displacement curve, and used to calibrate the parameters in the bi-linear bond-slip model. After Point 'B', the resistance is solely provided by the surface maximum friction (Fig. 4(e) and 4(f)). Therefore, the present analysis provides a useful tool to determine the parameters of the bilinear bond-slip model from simple pull-out tests as illustrated in the following section.

6. Calibration of control parameters

There are two bond-slip model parameters τ_f and δ_1 in the above analytical solution. They may be calibrated from the experimental load-displacement curve at the control points A(u_1, P_1), B(u_2, P_2) in Fig. 5. From Fig. 4(b) and Fig. 5, it is seen that

$$\delta_1 = u_1 \quad (42)$$

The value of τ_f can be obtained using two different methods in this analytical solution, which is dependent on the failure mechanism of pullout tests. When the failure mode is that the reinforcement is pulled out from the soil, τ_f can be obtained by substituting $P_u = P_2$ at Point 'B' into Eq. (39) and it can be expressed as below

$$\tau_f = \frac{P_2}{2b_g L} \quad (43)$$

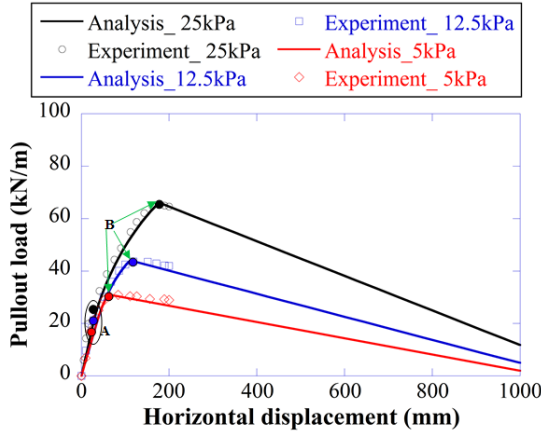


Fig. 6 Comparison of predicted load-displacement curve with Sieira *et al.*'s test data (Sieira *et al.* 2009)

On the other hand, when the failure mode is not the pull out mode, such as the rupture of reinforcement, the value of τ_f can be acquired by substituting $P_{ela-pla} = P_1$ and $\delta_1 = u_1$ at Point 'A' into Eq. (22), note that $\tanh(\lambda L) \approx 1$ under normal conditions. Thus, τ_f can be determined by combining Eq. (9) and Eq. (22) as below. Note that this method can also be used to obtain τ_f in the case of pullout mode.

$$\tau_f = \frac{P_1^2}{2b_g^2 u_1 E_g t_g} \quad (44)$$

Once the values of τ_f and δ_1 are obtained, then the full-range pullout behavior of geosynthetics, such as displacement distribution, interfacial shear stress and axial stress of geosynthetics, can be described using Eqs. (13)-(15), (29)-(34). The load-displacement curves in every loading stage can also be acquired as well.

7. Comparison with pullout test results

In this section, the key material parameters are calibrated following the above procedure for pullout tests of geosynthetics. They are then used to predict the whole load-displacement behavior and internal displacement distribution along the bond length. The predictions are compared with the test results.

7.1 Load-displacement relationship

Several pullout tests of geogrid reinforced soil were conducted by Sieira *et al.* (2009). The geometrical and material properties were: $b_g=1.0$ m, $t_g=0.35$ mm, $L=1.0$ m and $E_g=1.6$ GPa, among which, t_g is obtained by the equivalent stiffness method. The test load-displacement data are shown as markers in Fig.6 where the control points were identified as points A, B. The bond-slip parameters τ_f , δ_1 and the effective bond length $l_{e,e}$, which are calibrated following the above procedure, can be obtained as 32.6 kPa, 17.8 mm and 0.78 m under the normal stress of 25 kPa, 21.8 kPa, 17.7 mm and 0.95 m under the normal stress of 12.5 kPa, 15.5 kPa, 12.6 mm and 0.96m under the normal stress of 5kPa, respectively. The predicted load-displacement curve

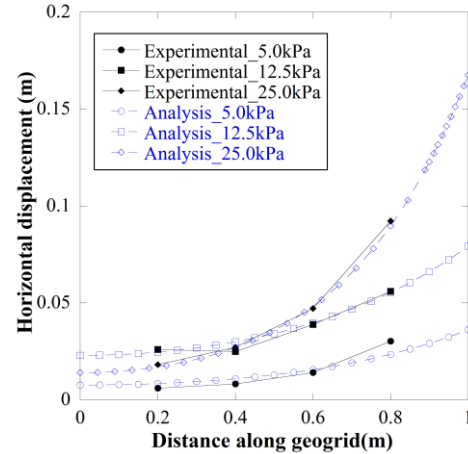


Fig. 7 Comparison of predicted internal displacement with Sieira *et al.*'s test data (Sieira *et al.* 2009)

using the parameters is plotted as the solid line in Fig. 6. It is clear that the present analytical solution reproduces closely the full non-linear behavior of the geogrid tested. It should be noted that the linear decrease in the debonding zone is deduced from Eqs. (40) and (41), and the slope of the curve can be obtained as $-2b_g\tau_f$, which is independent of pulling speed in pullout tests. However, in fact, the shape of the curve is dependent on the pulling speed.

7.2 Internal displacement distribution

Knowing the bond-slip model parameters τ_f and δ_1 , the internal displacement can be calculated using Eqs. (13), (29), (32), and (40) according to the stress states (I, II, III). Fig. 7 shows a comparison between the calculated internal displacement and the test data reported by Sieira *et al.* (2009) at the state of peak pullout loads under different normal stress. It can be seen clearly that the distribution of the calculated displacement closely matches the experimental results. The internal displacement of the reinforcement decreases gradually from the loading end to the free end. Also, the load end can bear a larger horizontal displacement with the increase of the normal stress, that is to say the larger normal stress improves the ductility as well as the ultimate load. This phenomenon can also be seen clearly from Fig. 6.

8. A parametric study

A parametric study was conducted to investigate the influences of the anchorage length, the axial stiffness of the reinforcement, the interfacial shear stiffness and the interfacial shear strength on the load-displacement relations and the ultimate load. The parameters of Sieira *et al.* (2009)'s experiment as given in Section 7.1 were used as the reference values.

8.1 Effect of anchorage length L

Fig. 8 shows the load-displacement curves calculated using different anchorage length L with $L > L_e$. It is found

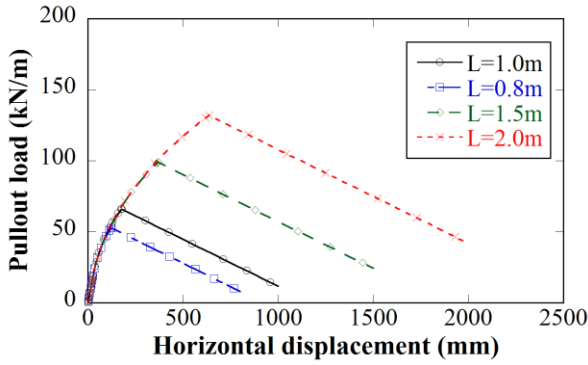


Fig. 8 Effect of the anchorage length on the load-displacement relationship

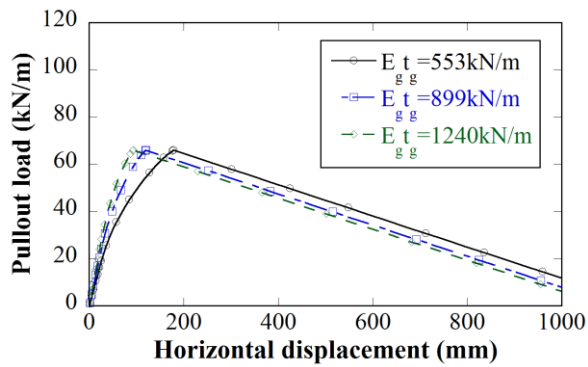


Fig. 9 Effect of the reinforcement axial stiffness on the load-displacement relationship

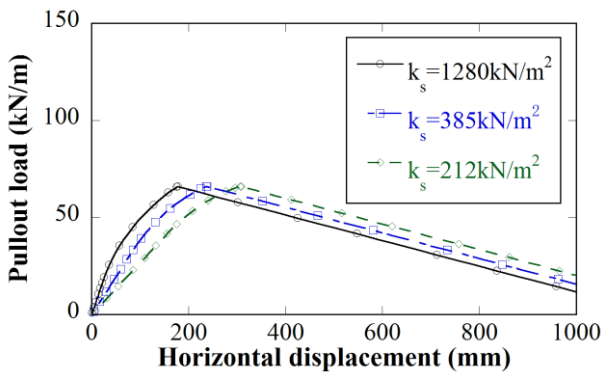


Fig. 10 Effect of the interfacial shear stiffness on the load-displacement relationship

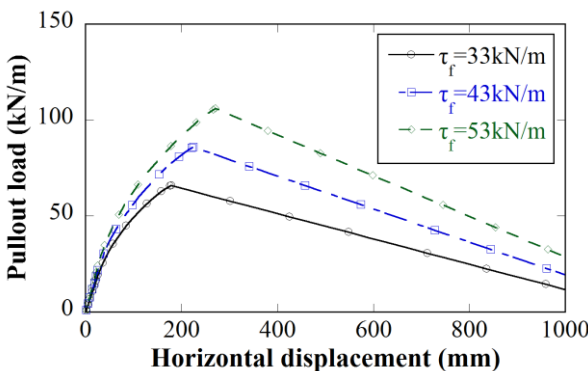


Fig. 11 Effect of the interfacial shear strength on the load-displacement relationship

that the curves in the elastic stage are independent of the anchorage length. In the elastic-plastic stage, the load continues to increase with the displacement. The hardening phenomenon is due to the existence of a constant shear strength τ_f after entering the elastic-plastic stage in the adopted bi-linear bond-slip model. It is also clear that a longer anchorage length improves the ductility as well as the ultimate load.

8.2 Effect of the reinforcement axial stiffness

Fig. 9 shows the influence of axial stiffness of the reinforcement on the pullout load-displacement relationship. It is clearly seen that the ductility decreases with the increase in reinforcement axial stiffness, and the ultimate pullout load remains constant for different axial stiffness.

8.3 Effect of the interfacial shear stiffness

Fig. 10 shows the effect of interfacial shear stiffness between reinforcement and the soil on the pullout load-displacement behavior. It can be clearly seen that the ductility increases but the ultimate pullout load remains relatively unchanged as the interfacial shear stiffness increases.

8.4 Effect of the interfacial shear strength

Fig. 11 shows the effect of reinforcement-soil interfacial shear strength on the pullout load-displacement relationship. With increase in interfacial shear strength, the ultimate pullout load and the ductility clearly increase. Moreover, it can be clearly seen that the larger is the interfacial shear strength, the smaller is the pullout displacement under the same pullout load before the interface debonds.

9. Conclusions

MSE structures have been widely used in slope and road engineering to retain unstable soil mass and save construction cost. Based on a bi-linear bond-slip model, a closed-form solution for predicting the full-range behavior of reinforcements under tension has been presented in this paper. Its practical meaning is that, once the bond-slip model is calibrated using the analytical solution from simple pullout tests, it can be subsequently used in numerical simulation of complicated engineering problems. The conclusions can be obtained as below.

(1) Explicit formulations for the shear stress and the shear slip at soil-reinforcement interface, the load-displacement relations, and the axial stress in the reinforcement, have been derived for each of the three distinct loading stages. All the control parameters in the solution are physical entities and can be directly calibrated from pullout test data.

(2) Three pullout tests with different normal stress were analysed using the developed solution. It was found that the predicted results are in good agreement with the experimental data in terms of load-displacement curve and internal shear displacement distribution. Thus the developed

solution offers a rigorous theoretical basis for understanding the full mechanical behavior of sheet-like reinforcements under tension.

(3) As an extension of the developed solution, parametric analyses were conducted on the load-displacement relations and the ultimate load of the pullout test. It was found that a longer anchorage length and a larger interfacial shear strength can improve the ductility as well as the ultimate load, and ductility reduces with increase in reinforcement axial stiffness and decrease in interfacial shear stiffness.

Acknowledgments

This study was supported by National Natural Science Foundation of China (41302221, 41001331), Research Fund for the Doctoral Program of Higher Education of China (20120072120033), the Fundamental Research Funds for the Central Universities (20140800) and Opening fund of State Key Laboratory of Geohazard Prevention and Geoenvironment Protection (SKLGP2017K020). The authors wish to express their sincere thanks to Prof. Z. J. Yang of Zhejiang University for his kind help in analytical analysis.

References

- Abdi, M.R. and Zandieh, A.R. (2014), "Experimental and numerical analysis of large scale pull out tests conducted on clays reinforced with geogrids encapsulated with coarse material", *Geotext. Geomembr.*, **42**(5), 494-504.
- Abramanto, M. and Whittle, A.J. (1995), "Analysis of pullout tests for planar reinforcements in soil", *J. Geotech. Eng.*, **121**(6), 476-485.
- Alobaidi, I.M., Hoare, D.J. and Ghataora, G.S. (1997), "Load transfer mechanism in pull-out tests", *Geosynth.*, **4**(5), 509-521.
- Bathurst, R.J. and Ezzein, F.M. (2015), "Geogrid and soil displacement observations during pullout using a transparent granular soil", *Geotech. Test. J.*, **38**(5), 673-685.
- Bergado, D.T., Voottipruex, P., Srikongsri, A. and Teerawattanasuk, C. (2001), "Analytical model of interaction between hexagonal wire mesh and silty sand backfill", *Can. Geotech. J.*, **38**(4), 782-795.
- Ferreira, J.A.Z. and Zornberg, J.G. (2015), "A transparent pullout testing device for 3D evaluation of soil-geogrid interaction", *Geotech. Test. J.*, **38**(5), 686-707.
- Ingold, T.S. (1982), *Reinforced Earth*, Thomas Telford, London, U.K.
- Karpurapu, R. and Bathurst, R.J. (1995), "Behavior of geosynthetic-reinforced soil retaining walls using the finite-element method", *Comput. Geotech.*, **17**(3), 279-299.
- Palmeira, E.M. (2009), "Soil-geosynthetic interaction: Modelling and analysis", *Geotext. Geomembr.*, **27**(5), 368-390.
- Ren, F.F., Yang, Z.J., Chen, J.F. and Chen, W.W. (2010), "An analytical analysis of the full-range behaviour of grouted rockbolts based on a tri-linear bond-slip model", *Construct. Build. Mater.*, **24**(3), 361-370.
- Schlosser, F. and Elias, V. (1978), "Friction in reinforced Earth", *Proceedings of the Symposium on Earth Reinforcement*, Pittsburgh, Pennsylvania, U.S.A., April.
- Sieira, A.C.C.F., Gerscovich, D.M.S. and Sayão, A.S.F.J. (2009), "Displacement and load transfer mechanisms of geogrids under pullout condition", *Geotext. Geomembr.*, **27**(4), 241-253.
- Teerawattanasuk, C., Bergado, D. and Kongkitkul, W. (2003), "Analytical and numerical modeling of pullout capacity and interaction between hexagonal wire mesh and silty sand backfill under an in-soil pullout test", *Can. Geotech. J.*, **40**(5), 886-899.
- Wang, Z., Jacobs, F. and Ziegler, M. (2016), "Experimental and DEM investigation of geogrid-soil interaction under pullout loads", *Geotext. Geomembr.*, **44**(3), 230-246.
- Weerasekara, L. and Wijewickreme, D. (2010), "An analytical method to predict the pullout response of geotextiles", *Geosynth.*, **17**(4), 193-206.
- Wilson-Fahmy, R.F. and Koerner, R.M. (1993), "Finite element modelling of soil-geogrid interaction with application to the behavior of geogrids in a pullout loading condition", *Geotext. Geomembr.*, **12**(5), 479-501.
- Wilson-Fahmy, R.F., Koerner, R.M. and Sansone, L.J. (1994), "Experimental behavior of polymeric geogrids in pullout", *J. Geotech. Eng.*, **120**(4), 661-677.
- Xu, C., Chen, H., Shi, Z. and Ren, F. (2013), "Research on the mechanical behavior of soil-reinforcement interface by horizontal cyclic shear test", *Rock Soil Mech.*, **34**(6), 1553-1559.
- Yang, G., Ding, J., Zhou, Q. and Zhang, B. (2010), "Field behavior of a geogrid reinforced soil retaining wall with a wrap-around facing", *Geotech. Test. J.*, **33**(1), 1-6.

CC